pubs.acs.org/acschemicalbiology

Articles

Mitochondria-Associated Transcriptome Profiling via Localizable Aggregation-Induced Emission Photosensitizers in Live Cells

Jiying Liang, Jinghua Han, Yuan Zhuang, GuanHua Chen, and Ying Li*

Cite This: https://doi.org/10.1021/acschembio.3c00617

Read Online

ACCESS | Metrics & More | Article Recommendations | Supporting Information

ABSTRACT: In recent decades, there has been increasing interest in studying mitochondria through transcriptomic research. Various exogenous fusion protein-based proximity labeling methods have been reported that focus on the site of one particular protein/peptide and might also influence the corresponding localization or interactome. To enable unbiased and high spatial-resolution profiling of mitochondria-associated transcriptomes in live cells, a flexible RNA proximity labeling approach was developed using aggregation-induced emission (AIE) type photosensitizers (PSs) that possess great mitochondria-targeting capabilities. Their accumulation in an enclosed mitochondrial environment tends to enhance the fluorescence emission and reactive oxygen species generation. By comparing the in vitro optical properties, photosensitization processes, as well as the in cellulo mitochondrial specificity and RNA labeling performance of four AIE PSs, high-throughput sequencing analysis was conducted using TFPy-mediated RNA proximity labeling in live HeLa cells. This approach successfully captured a comprehensive list of transcripts, including mitochondria-encoded RNAs, as well as some nuclear-derived RNAs located at the outer mitochondrial membrane and interacting organelles. This small molecule-based proximity labeling method bypasses complex genetic manipulation and transfection steps, making it readily applicable for diverse research purposes.

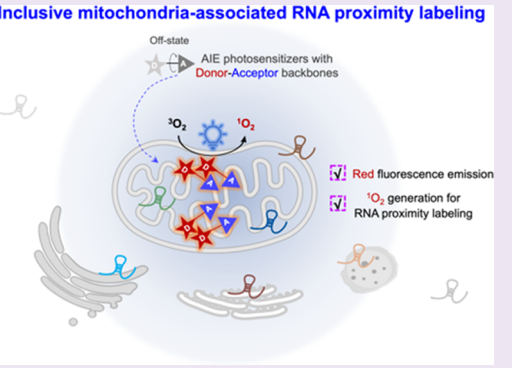

Downloaded via UNIV OF HONG KONG on February 7, 2024 at 02:52:22 (UTC).
See https://pubs.acs.org/sharingguidelines for options on how to legitimately share published articles.

INTRODUCTION

Mounting transcriptomic research suggests that the precise RNA localization at the right time is crucial for their biological functions within eukaryotic cells.[1,2] To investigate the asymmetric distribution of RNA species with high temporospatial resolution, proximity labeling-based approaches have rapidly evolved over the past decade.[3,4] However, many existing methods rely on the expression of exogenous proteins for locally generating reactive intermediates, such as APEX2,[5] HaloTag,[6] and miniSOG.[7] The corresponding stable cell line construction can be time-consuming and potentially affect the function of target proteins or their interactomes.[5,7,8] To overcome these limitations, the development of entirely chemical photosensitizers (PSs) with specific targeting capabilities and sufficient singlet oxygen ($^1O_2$) yield is a promising approach.[4,9] In this regard, we have reported a chemical PS-based proximity labeling method to capture RNAs and proteins near chromatin in live cells, where a classic PS, dibromofluorescein was coupled with Hoechst, a known nucleus-targeting motif.[10] This combination was also utilized by Hamachi's group to profile nuclear proteins.[11]

In recent decades, mitochondria-associated transcriptomes have received numerous attention,[12,13] due to the multifaceted roles of mitochondria in various biological processes, such as ATP production, redox balance, and cell survival/apoptosis.[14,15] These processes depend on the intricate engagement of diverse RNAs and proteins encoded by both mitochondrial and nuclear genomes.[16,17] Several methods have been adopted to characterize mitochondria-related RNAs, including mitochondrion isolation followed by high-throughput sequencing,[12,18] APEX2-based RNA-protein cross-linking,[19] as well as direct RNA proximity labeling using APEX2 and miniSOG.[5,7,18,19] While these proximity labeling techniques offer better spatial resolution over mitochondrial isolation, they often focus on specific mitochondrial sites or proteins, limiting an impartial interpretation of mitochondria-associated transcripts at one time. In addition, the expression of fusion proteins required by these methods might not be feasible in certain cell lines or biological samples. Therefore, it is crucial to exploit convenient chemical tools that enable unbiased deciphering of mitochondria-associated transcriptomes in live cells.

Cationic mitochondria-targeting PSs are potential candidates to achieve mitochondria-associated transcriptome analysis. The efficient and specific mitochondrial uptake of these PSs relies on the synergistic effect of proper lipophilicity and the negative

Received: October 6, 2023
Revised: January 10, 2024
Accepted: January 11, 2024

ACS Publications © XXXX American Chemical Society

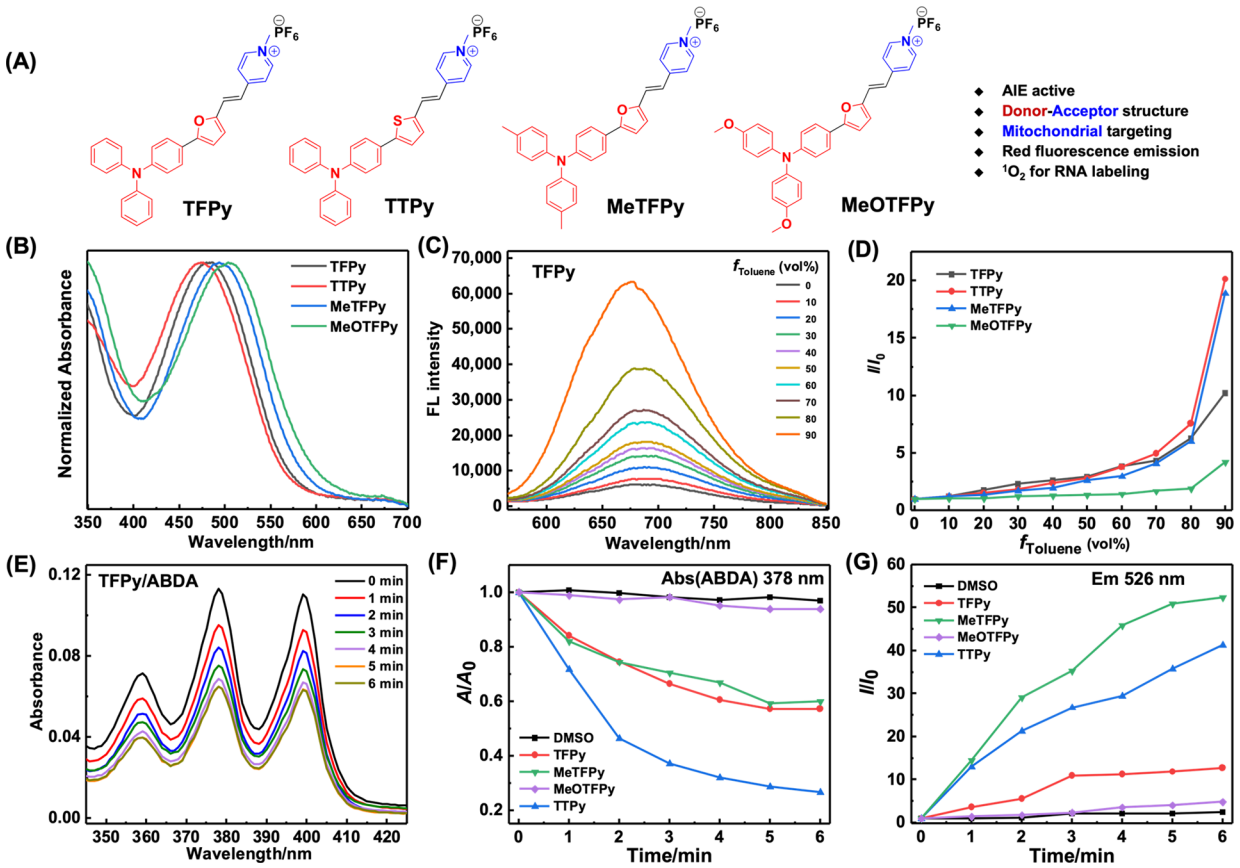

Figure 1. (A) Molecular structures of the investigated AIE PSs. (B) Normalized absorption spectra of each PS in DMSO solution. (C) Fluorescence (FL) spectra of 10 μM TFPy in DMSO/toluene mixtures with different toluene fractions ($f_{Toluene}$). λ_{ex}: 484 nm. (D) Plots of the relative FL intensity of 10 μM each PS versus $f_{Toluene}$, where I_0 and I are the peak values of FL intensities in DMSO and DMSO/toluene mixtures. (E) Alterations for absorption spectra of ABDA in the presence of TFPy upon different durations of blue light irradiation (37 mW/cm^2). [ABDA]: 100 μM; [PS]: 3.5 μM. (F) Decomposition process of ABDA with light irradiation time in the presence of different PSs, where A_0 and A are the absorbance of ABDA at 378 nm before and after light irradiation, respectively. DMSO group was set as the negative control. (G) Fluorescence enhancement process of DHR 123 with the light irradiation time in the presence of different PSs, where I_0 and I are the fluorescence emission before and after light irradiation, respectively. [DHR 123]: 10 μM; [PS]: 1 μM. λ_{ex}: 490 nm; λ_{em}: 526 nm. DMSO group was set as the negative control.

inner mitochondrial membrane (IMM) potential ($\Delta\Psi_m$).[20,21] Notably, aggregation-induced emission (AIE) active PSs with mitochondria-targeting abilities have received increasing attention in view of their good photostability, high signal-to-noise ratio, and efficient generation of reactive oxygen species (ROS).[21−23] In dilute and soluble conditions, AIE PSs exhibit minimal luminescence but emit strong luminescence in poor solvents and solid state. This is because intramolecular vibration or rotation events are restricted, reducing non-irradiative decay and increasing the excitons available for either fluorescent emission (singlet excitons) or photosensitization (triplet excitons) pathways.[22,23] This unique property enables enhanced intracellular imaging by accumulating AIE PSs within mitochondria and generating mitochondria-specific $^1O_2$ for proximity labeling.[24] Therefore, mitochondria-targeting AIE PSs hold the potential for profiling mitochondria-associated transcriptomes in diverse cell lines.

To demonstrate the feasibility, we selected and compared four AIE PSs for mitochondria-associated transcriptome analysis. We initially focused on two reported AIE PSs (Figure 1A, TFPy and TTPy) with the ability to target mitochondria and produce $^1O_2$. These PSs incorporate a donor−acceptor (D−A) scaffold composed of the electron-donating triphenylamine (TPA) moiety and the electron-withdrawing pyridinium cation.[25,26] TPA and its analogues, known as classic AIE-active motifs, feature nonplanar structures that disrupt intermolecular $\pi-\pi$ stacking in the aggregated state, resulting in enhanced emission.[27] The pyridinium cationic moiety not only acts as an electron acceptor but also serves as an effective mitochondria-targeting motif due to the $\Delta\Psi_m$.[28] To further increase the intramolecular D−A strength, an electron-rich heterocycle (such as furan or thiophene) and a carbon−carbon double bond were incorporated as the π-bridge components.[29,30] Furthermore, we designed two additional AIE PSs, MeTFPy and MeOTFPy, where methyl- or methoxy-TPA segments were introduced to enhance the D−A strength (Figure 1A). Increasing D−A strength generally leads to higher ROS generation yield, an outcome of more efficient separation between the highest energy occupied molecular orbital (HOMO) and the lowest energy unoccupied molecular orbital (LUMO), as well as a smaller energy gap (ΔE_{S1-T1}) between singlet (S_1) and triplet (T_1) excited states.[22,23,31]

RESULTS AND DISCUSSION

Photophysical Properties and In Vitro Photosensitization. The four AIE PSs (TFPy, MeTFPy, MeOTFPy, and

https://doi.org/10.1021/acschembio.3c00617
ACS Chem. Biol. XXXX, XXX, XXX−XXX

TTPy) were obtained within several synthetic steps with decent yields, and the details are available in the Supporting Information. The substitution of iodide with PF_6^- was implemented to prevent the formation of potentially hazardous byproducts, such as triiodide ions or molecular iodine.[32] With these PSs in hand, we proceeded to investigate their photophysical properties. The introduction of methyl and methoxy groups led to an increased D−A strength. Accordingly, the absorption peaks of TFPy, MeTFPy, and MeOTFPy in dimethyl sulfoxide (DMSO) solution exhibited a red-shifted pattern, with respective wavelengths of 484, 494, and 504 nm (Figure 1B). Density functional theory (DFT) calculations further supported these observations, indicating a progressively decreasing HOMO−LUMO energy gap among the three PSs (Figure S1). In contrast, TTPy exhibited a slightly blueshifted absorbance (474 nm), consistent with previously reported data,[25] despite its theoretically predicted smaller HOMO−LUMO energy gap according to our DFT calculations (Figure S1). This discrepancy could be attributed to the differences between the experimental absorbance measurements and the theoretical model. Nevertheless, HOMO−LUMO separation in all four PSs was also verified by DFT computation, where the HOMO is delocalized primarily at the TPA unit and the pyridinium moiety dominates the LUMO (Figure S1).

All four PSs exhibited AIE-type behaviors in terms of fluorescence emissions (Figures 1D and S2). In DMSO solutions, the PSs displayed weak fluorescent signals, with MeOTFPy being the least fluorescent (Figure S2A). This reduced fluorescence might result from the active rotation of the two methoxy units, leading to a more pronounced nonradiative decay in the soluble state. However, when the volume percentage of toluene in the solvent mixture ($f_{Toluene}$) was increased from 0 to 90%, we observed a progressive increase in red fluorescence emission with significant Stokes shifts (Figures 1C and S2, and Table S2). The final enhancement reached 10-, 19-, 4-, and 20-fold for TFPy, MeTFPy, MeOTFPy, and TTPy, respectively (Figure 1D). The stronger fluorescence signals with the higher $f_{Toluene}$ can be attributed to the restricted rotations of the PSs, reducing nonirradiative decay processes.

Subsequently, we evaluated the potential of the four PSs for proximity labeling by investigating their ROS generation. To assess $^1O_2$ production via the type II photochemical reaction, we employed 9,10-anthracenediylbis(methylene)dimalonic acid (ABDA).[33] The absorbance of ABDA at 378 nm decreases as it reacts with $^1O_2$ to specifically form an endoperoxide structure (Figure S3A). The decreasing absorption was monitored in the presence of the four AIE PSs with different durations of blue light irradiation (Figures 1E and S3). TTPy displayed the fastest rate of ABDA decomposition, while TFPy and MeTFPy exhibited similar kinetics (Figures 1F and S3). In contrast, MeOTFPy showed minimal $^1O_2$ production, comparable to the negative control of DMSO. Furthermore, we characterized the generation of two other types of ROS, namely, superoxide ion ($O_2^{\bullet-}$) and hydroxyl radical ($HO^{\bullet}$), which are derived from the type I photochemical reaction involving electron transfer (Figure 1G).[34,35] As depicted in Figures 1G and S4−S6, the $O_2^{\bullet-}$ and $HO^{\bullet}$ generation capabilities among the PSs were ranked as MeTFPy > TTPy > TFPy > MeOTFPy. These results suggested that the stronger electron-donating methoxy unit in MeOTFPy attenuated its ROS productivity for both type I and II photochemical reactions compared to the original TFPy structure.

To better comprehend the correlation between ROS generation and molecular structures, we integrated the analysis above with time-dependent density functional theory calculations (Figure S5F).[36] A smaller ΔE_{S1-T1} value commonly indicates a higher efficiency in ROS generation.[23] MeOTFPy showed the lowest ΔE_{S1-T1} value with its enhanced intersystem crossing (ISC) thanks to the strongest D−A strength. However, the nonradiative decay resulting from the vibration and rotation of the two methoxy groups might consume the excitons significantly, counteracting the effect of efficient ISC.[37] This assumption aligns well with the observed lower fluorescence signals and reduced ROS generation in both good and poor solvent systems (Figures 1D and S2A). In the case of MeTFPy, a relatively small ΔE_{S1-T1} value together with the highest radical generation efficiency (Figure 1G) suggested that the introduction of an electron-donating methyl group probably promotes ROS generation mainly through the type I reaction pathway. Compared to TFPy, TTPy exhibited a higher ROS yield, resulting from its slightly lower ΔE_{S1-T1} as well as the more efficient spin−orbit coupling between S_1 and T_1 states induced by the sulfur atom.[38]

In short, while incorporating D−A structure or larger atoms generally improves ROS generation, it is crucial to consider potential interference from other competing pathways when designing AIE-type PSs. These in vitro experiments on ROS generation also serve as a fundamental reference for subsequent in cellulo proximity labeling studies.

Mitochondria-Specific Subcellular Imaging. We proceeded to verify the mitochondria-targeting ability of the PSs via fluorescence confocal imaging in live cells. Considering the red emission of these PSs, we costained live Hela cells with each PS (1 μM or 5 μM) and MitoTracker Green FM for 30 min. As anticipated, the excellent colocalization of each PS with MitoTracker Green FM was observed (Figures 2, S7 and S9). Furthermore, the Pearson correlation coefficients between each PS and MitoTracker channel were all quantified to be above 0.8 (Figure S8), indicating their high specificity for mitochondria in Hela cells. The specificity was further supported through co-staining assays using endoplasmic reticulum (ER) tracker and lysosome tracker with either TFPy or MitoTracker Red CMXRos, respectively (Figures S10 and S11). In addition, we conducted dynamic light scattering assays in a 1% DMSO/99% H_2O mixture system to determine their size distribution of the PSs (Figure S12). Their average hydrodynamic diameters measured were below 100 nm (Figure S12B), hinting their sufficient cell permeability and the potential to accumulate inside mitochondria.[37,39]

Comparative Photoactivated Proximity Labeling via a Fluorescence Confocal Imaging Study. Following the effective targeting of mitochondria observed in live Hela cells, we subsequently assessed the labeling efficiency of these AIE PSs in the cellular environment through confocal imaging studies. The in cellulo labeling sites were conjugated with propargyl amine (PA) and further visualized through copper-(I)-catalyzed alkyne−azide cycloaddition (CuAAC) with TAMRA azide (TAMRA_N_3), shown in the green fluorescence channel (Figure 3). For mitochondrial staining, MitoTracker Deep Red 633 was used as it retains its signal after fixation due to the presence of a thiol-reactive chloromethyl group.[40] Compared to the negative controls (Figures 3B and S13), the presence of TFPy, MeTFPy, or

https://doi.org/10.1021/acschembio.3c00617
ACS Chem. Biol. XXXX, XXX, XXX−XXX

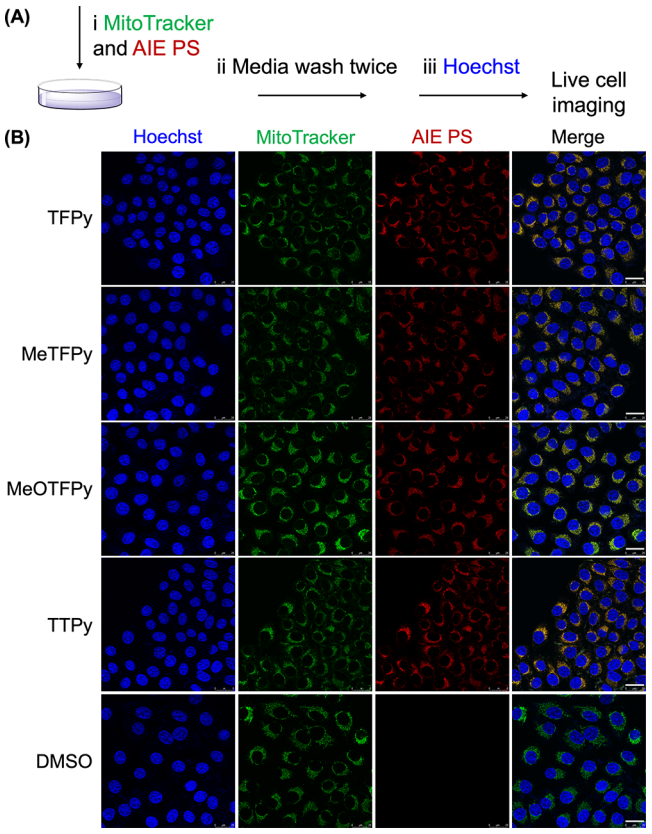

Figure 2. Fluorescence confocal live cell imaging. (A) Scheme of the procedure for live cell staining. (B) Representative fluorescence confocal images of live Hela cells incubating with 1 μM each PS or equal volume DMSO (negative control) and 50 nM MitoTracker Green FM. Hoechst was used as the nuclear marker, shown as blue signals; MitoTracker Green FM was represented as green signals; the subcellular distribution of each PS was shown as red signals. Scale bar: 25 μm.

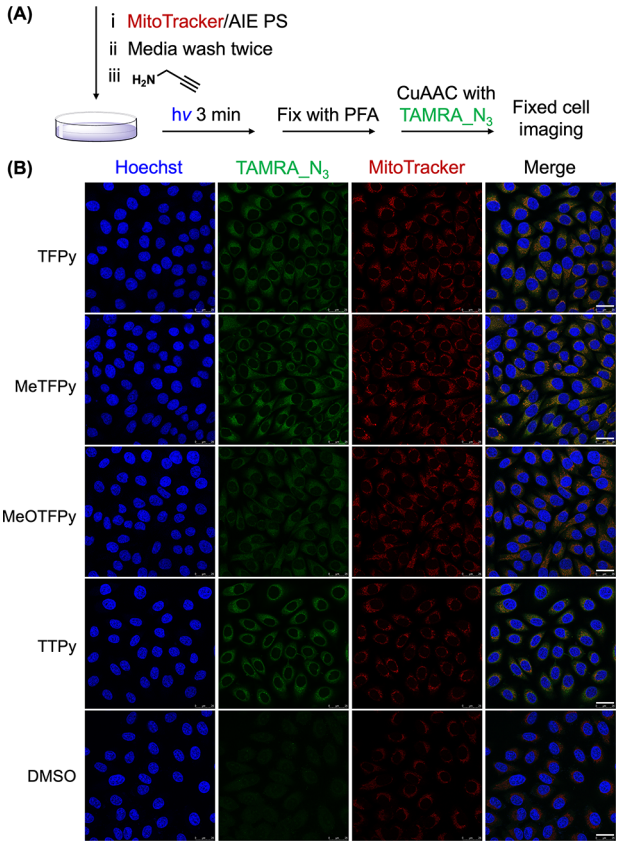

Figure 3. Fluorescence confocal imaging analysis after in cellulo labeling. (A) Scheme of the procedure from live cell labeling, cell fixing, slide workup, to imaging assay. (B) Representative fluorescence confocal images upon each PS-mediated proximity labeling (5 μM) in Hela cells. Hoechst was used as the nuclear marker, shown as blue signals; the labeled sites were visualized via CuAAC with the TAMRA fluorophore, shown as green signals; MitoTracker Deep Red 633 was represented as red signals. Scale bar: 25 μm.

MeOTFPy along with light irradiation resulted in spatially overlapping fluorescence signals between TAMRA and Deep Red channels, implying mitochondria-restricted $^1O_2$ generation (Figure 3B). However, TTPy-mediated labeling demonstrated a small amount of diffused TAMRA signals beyond the boundary of the MitoTracker signals (Figures 3B and S14 for enlarged images). Such signal diffusion pattern was less obvious when a lower concentration of TTPy or a shorter irradiation period was applied (Figure S15). This phenomenon can be attributed to the much higher $^1O_2$ yield of TTPy, causing background labeling outside mitochondria.

To elucidate the primary type of ROS involved in the photoactivable proximity labeling mediated by the listed PSs, we employed several ROS scavengers in confocal imaging studies. Sodium azide (NaN_3) and trolox, known to quench $^1O_2$,[41,42] were used during in cellulo labeling, respectively. The presence of the two scavengers resulted in a significant reduction of TAMRA signals for all four PSs (Figures S16–S19), close to the level of negative controls. When cells were incubated with tiron or mannitol, known scavengers of $O_2^{\bullet-}$ and $HO^{\bullet}$, respectively,[43,44] some attenuations at TAMRA channel were observed (Figures S16–S19). However, the quenching effects were not as pronounced as those observed with the $^1O_2$ scavengers (Figure S20). Consistent with the much lower $^1O_2$ yield of MeOTFPy in vitro (Figures 1E and S3), we also noted lower TAMRA signals under MeOTFPy-mediated labeling conditions (Figure S18). Collectively, the imaging data strongly suggested that $^1O_2$ was the central ROS responsible for mitochondria-restricted biomolecular tagging mediated by the four PSs in the presence of PA.

Photoactivated RNA Proximity Labeling. We conducted dot blot analysis to examine the proximity labeling mediated by the AIE PSs at the RNA level. For the in vitro RNA labeling assay, a mixture of total RNA, each AIE PS and PA was exposed to blue light irradiation for 3 min in an Eppendorf tube. The labeled RNA underwent biotinylation via CuAAC (Figure S21A) and the stronger biotinylation signal indicated the higher RNA labeling efficiency. The in vitro study revealed the following trend: TTPy ≫ TFPy > MeTFPy > MeOTFPy (Figure S21B,C), which correlated with their respective $^1O_2$ generation capabilities shown in Figure 1F. Similarly, in the in cellulo labeling experiment, RNA was processed and biotinylated as the in vitro assay (Figure S22A). The in cellulo study reflected the following RNA labeling efficiency: TTPy ≫ MeTFPy > TFPy > MeOTFPy (Figure S22B,C). The comparison of the in vitro and in cellulo RNA labeling assay indicated that MeTFPy might produce slightly more $^1O_2$ inside the mitochondria of live cells compared to TFPy. This observation might result from the higher AIE effect

https://doi.org/10.1021/acschembio.3c00617
ACS Chem. Biol. XXXX, XXX, XXX−XXX

(Figure 1D) or the increased accumulation of MeTFPy within mitochondria.

Cytotoxicity and Labeling Specificity of AIE PSs. In addition to the labeling efficiency, we assessed the cytotoxicity of these PSs under both dark and light irradiation conditions. After 0 or 3 min of blue light irradiation, the Hela cells were cultured in the growth media for 24 h and then incubated with a solution of methylthiazolyldiphenyltetrazolium bromide (MTT) for 4 h. As depicted in Figure S23, all four PSs demonstrated good biocompatibility and exhibited minimal dark cytotoxicity across the tested concentration range. However, upon 3 min blue light exposure, cell viability displayed a dose-dependent reduction for each PS due to the increasing ROS generation. Comparing their cytotoxicity at the same concentration (5 μM), we observed that TTPy resulted in more pronounced cell death, followed by MeTFPy, TFPy, and MeOTFPy, respectively. Overall, the trends shown in MTT assays were consistent with the results of photoactivated ROS generation.

Combining the results from confocal imaging, dot blot, and cytotoxicity studies, we proceeded to perform quantitative reverse transcription polymerase chain reaction (RT-qPCR) analysis to evaluate the RNA labeling specificity using TFPy and MeTFPy (Figure 4). Upon 3 min light irradiation, several

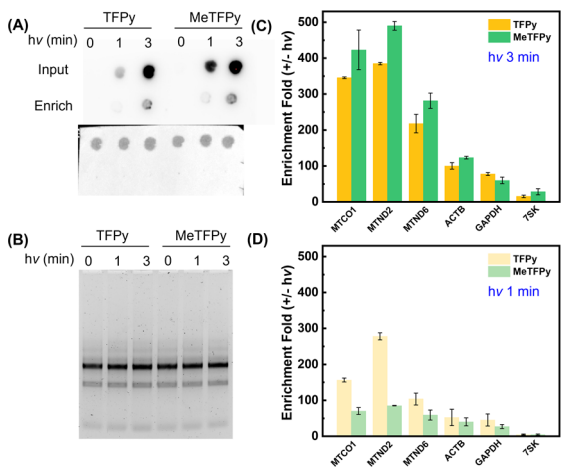

Figure 4. (A) Dot blot analysis of enrichment based on the biotinylated RNAs via CuAAC at TFPy (5 μM) or MeTFPy (5 μM) mediated labeling conditions. (B) Agarose gel analysis of RNA integrity after TFPy- or MeTFPy-mediated labeling and the CuAAC reaction. RT-qPCR analysis of streptavidin-enriched RNAs from TFPy- and MeTFPy-mediated labeling under (C) 3 and (D) 1 min light irradiation duration, with three mtRNAs as the positive controls, the two cytoplasmic mRNAs ACTB and GAPDH, and the nuclear long noncoding RNA 7SK as the negative markers in biologically duplicate experiments. The enrichment was calculated against a no-hν negative control using the $\Delta\Delta$Ct method.

mitochondria-encoded RNAs (mtRNAs: MTCO1, MTND2, and MTND6) demonstrated significant enrichment. In contrast, the enrichment of two cytoplasmic mRNAs (ACTB[45] and GAPDH[46]) was less pronounced. Furthermore, the nuclear long noncoding RNA 7SK[47] exhibited minimal enrichment (Figure 4C). A comparable trend in the recovery yield was also detected for TFPy-mediated labeling (Figure S25). Additionally, RT-qPCR analysis upon 1 min blue light exposure displayed a noticeable decrease in the absolute enrichment fold of all inspected RNAs, due to the lower RNA biotin signals and less efficient RNA enrichment (Figure 4A,D). Contrary to our expectation, MeTFPy did not demonstrate relatively improved enrichment of mtRNAs compared to that of TFPy in terms of various negative reference markers (Figure 4C,D). This observation was inconsistent with the higher RNA labeling efficiency of MeTFPy (Figure 4A), and its similar spatial resolution of proximity labeling compared to TFPy (Figures 3B and S24). The exact reasons MeTFPy exhibited a lower spatial resolution under shorter light exposure remain unclear (Figure 4D).

Moreover, considering the covalent conjugation of PA onto biomolecules during the labeling procedure, we compared the cell viability in the absence and presence of PA for both TFPy and MeTFPy upon blue light irradiation (Figure S26). No additional perturbance was observed upon PA modification in the Hela cells. The cell viability remained higher when cells were treated with TFPy compared to MeTFPy, which can be attributed to the greater generation of radicals by MeTFPy via the type I pathway (Figures 1G, S5 and S6). Collectively, TFPy demonstrated more reliable labeling specificity and lower cytotoxicity, making it the ideal candidate for mapping mitochondria-associated RNAs in live cells.

Identification of Mitochondria-Associated Transcriptomes. To obtain a comprehensive understanding of TFPy-mediated RNA labeling, we extended our analysis to the transcriptome level. Live Hela cells were labeled with 2.5 and 5 μM TFPy, respectively, and the RNAs were subsequently biotinylated via CuAAC. The RNA samples collected before streptavidin−biotin pulldown were dedicated to "Input" libraries, while the RNA samples obtained after pulldown were constructed into "Enrich" libraries. All libraries were prepared after rRNA depletion, and the reproducibility of our results was confirmed by the strong correlation observed within the "Input" and "Enrich" samples (Figure S27). To assess the influence of blue light illumination on transcription quantification, we compared the "Input" sample-based libraries between 3 and 0 min irradiation groups. Minimal variance was observed between the two conditions across the biological triplicates, indicating the low disturbance from blue light exposure and the simultaneous production of $^1O_2$ during the labeling procedure (Figure S27). Ranking based on the enrichment fold change between "Enrich" and "Input" libraries, the top 300 candidates (adjusted-P value < 0.05) were identified as enriched transcripts under each labeling condition (Figure S28). The overlap between the two enriched lists reaches up to 80%, including 241 RNAs showing slightly higher enrichment under the 5 μM TFPy labeling conditions (Figures 5A and S28C). We also noticed that in the case of 2.5 μM TFPy_data, the enriched transcripts had higher confidence levels (Figure S28B), indicating that a low supply of $^1O_2$ can potentially narrow the labeling range and provide more convincing information.

Among the overall differentially expressed genes (DEGs), mtRNAs exhibited much higher enrichment than nuclear-encoded RNAs irrespective of TFPy concentrations (Figure 5B), which is consistent with our confocal imaging analysis and RT-qPCR results (Figures 2−4). Representatively, the genome tracks of one mtDNA gene (*MTND5*) and one nuclear-encoded mitochondrial-related gene (*CPS1*)[48] under two labeling conditions suggested their good enrichment, while the sequencing reads mapped to *GAPDH* gene, encoding a cytoplasmic mRNA,[46] showed minimal variation between the "Input" and "Enrich" samples (Figure S28D). Furthermore,

https://doi.org/10.1021/acschembio.3c00617
ACS Chem. Biol. XXXX, XXX, XXX−XXX

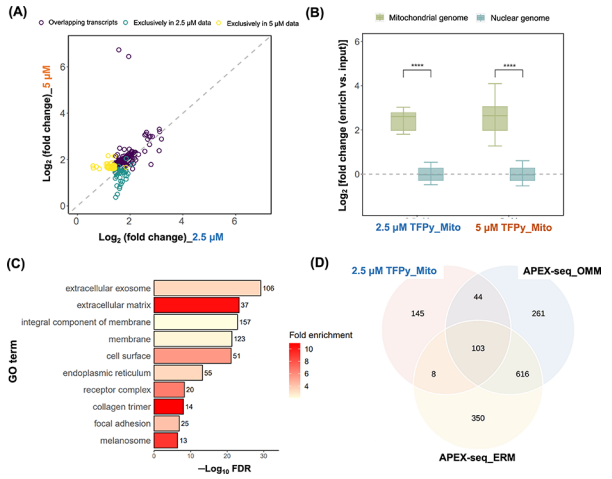

Figure 5. (A) Scatter plot of $\log_2$ (fold change) comparison of the top 300 enriched transcripts between 5 μM (Y-axis) vs 2.5 μM (X-axis) TFPy data. Purple circles represented the overlapping enriched transcripts under two conditions; yellow circles represented the transcripts exclusively included in 5 μM_TFPy data; green circles represented the transcripts exclusively included in 2.5 μM_TFPy data. (B) Box whisker plot of enrichment for transcripts derived from mitochondrial and nuclear genomes, respectively, in our two data sets at the two labeling conditions. Data were analyzed via the Wilcox test, with ****P < 0.0001. (C) Top 10 most significant GOCC terms enriched by the top 300 DEGs identified in 5 μM TFPy labeling condition. The number of transcripts in each GO term was marked. (D) Venn diagram showing the overlap between the top 300 DEGs under 2.5 μM TFPy labeling condition and the published OMM and ERM-enriched transcripts identified by APEX-seq.

despite both data sets being derived from rRNA-depletion libraries, we noticed the remarkable enrichment of 2 mtrRNAs with 5 μM TFPy (Figures 5A and S28A). Several mttRNAs also displayed an obvious enrichment in our data analysis, although small transcripts are generally excluded during our size selection procedure (Figure S28). The enrichment patterns for mtrRNAs and mttRNAs were consistent with the reported study.[19]

Gene ontology cellular components (GOCC) enrichment analysis of the top 300 DEGs identified with TFPy implied that many enriched transcripts were involved in membrane-, extracellular exosome-, and ER-related terms (Figures 5C and S29A). Although not as prominently as the other terms, our approach also yielded significant enrichment of GOCC terms related to mitochondria (Figure S29B,C). The above transcriptome analysis alluded that TFPy-mediated RNA proximity labeling covers not only transcripts within mitochondria but also those at the mitochondria outer membrane (OMM), as well as the interacting organelles. Given that commercial mitochondrial trackers are reported to accumulate at the IMM,[49,50] the colocalization imaging data (Figures S7, S10, and S11) suggest that TFPy predominantly locates at the IMM as well. While the gap between IMM and OMM is 20−22 nm,[51,52] shorter than the intracellular diffusion radius of $^1O_2$ (~70 nm),[53] OMM is also porous for small molecules with molecular weight <5 kDa.[54] Therefore, we inferred that in situ generated $^1O_2$ could cross mitochondrial membranes to label mtRNAs in the mitochondrial matrix as well as nuclear-derived transcripts in the proximity outside mitochondria. When comparing our two data sets with the reported OMM data obtained via APEX-seq,[5] a notable overlap was observed in the identified transcripts, suggesting the inclusive labeling pattern of TFPy (Figures 5D and S29D). Furthermore, the evident overlap between our mitochondria-enriched transcripts and ER membrane (ERM)-enriched transcripts identified by APEX-seq[5] (Figures 5D and S29D) provides additional support for our hypothesis that the intimate interactions between mitochondria and other organelles[55,56] facilitate the labeling process to occur on RNAs present at these interacting organelles. Hence, TFPy/$^1O_2$-mediated proximity labeling allows for the capture of most mtRNAs inside mitochondria as well as many nuclear-encoded transcripts adjacent to the OMM and mitochondria-interacting organelles.

CONCLUSIONS

To summarize, we explored and compared four AIE PSs with mitochondria-targeting capabilities for RNA proximity labeling in live cells. Among these PSs, TFPy exhibited a favorable balance between acceptable $^1O_2$ yield and low cytotoxicity under light irradiation thanks to its moderate D−A strength. Both comparative confocal imaging analysis and RT-qPCR assay indicated that TFPy demonstrated superior specificity for mitochondria. Moreover, our transcriptome analysis revealed that TFPy-mediated labeling captured a significant portion of mtRNAs regardless of the TFPy concentration used. Notably, in addition to transcripts in the mitochondrial matrix, TFPy/$^1O_2$-mediated proximity labeling exhibited a broader coverage of mitochondria-associated transcripts localized at the OMM and interacting organelles. This inclusive labeling feature of TFPy aligns well with its main accumulation at IMM and the relatively larger diffusion radius of $^1O_2$ compared to the distance between OMM and IMM. The $^1O_2$-driven mechanism is consistent with those of previously reported synthetic and genetic encoded PSs,[9,10,57] thus allowing for both RNA and protein proximity labeling (Figure S30). Consequently, we envision that such a small molecule-based approach for mitochondria-associated proximity labeling can offer a compressive evaluation of mitochondrial status in various cell lines of interest. This general approach complements other methods with a more specialized focus.

METHODS

Cell Culture. Hela cells (ATCC) were cultured in DMEM supplemented with 10% FBS, 1% penicillin/streptomycin, and grown at 37 °C and 5% CO_2.

Live Cell Fluorescence Confocal Imaging. Cells were seeded and cultured at 37 °C in a 35 mm glass-bottomed dish. After cells grew to about 70% confluence, each AIE PS and MitoTracker Green FM (50 nM, Thermo Fisher, cat. no. M7514) in HBSS buffer were adopted to co-stain cells for 30 min at 37 °C, 5% CO_2. Then, the cells were washed with fresh media twice (each for 20 min) and stained with Hoechst for 5 min. Imaging analysis was carried out on the Leica Confocal Microscope.

Photo-Oxidation Biomolecular Labeling via Fluorescence Confocal Imaging after CuAAC. Cells were seeded at equal density in a 6-well cell culture dish with one glass coverslip in each well and grew to about 70% confluence. Cells were initially coincubated with each AIE PS (5 μM in HBSS buffer, DMSO% ≤ 0.5%), and MitoTracker Deep Red 633 (1 μM, Thermo Fisher, cat. no. M22426) for 30 min at 37 °C, 5% CO_2 and replaced with fresh media for 20 min twice. Cells were then incubated with 2 mM PA in HBSS buffer for 2 min at 37 °C, 5% CO_2, and irradiated for 3 min with blue light at RT. Cells were washed by Dulbecco's phosphate-buffered saline (DPBS) buffer twice. The unlabeled controls were processed in the same way, except that light irradiation was omitted or AIE PSs were

https://doi.org/10.1021/acschembio.3c00617
ACS Chem. Biol. XXXX, XXX, XXX−XXX

replaced by equal volume DMSO. Then, the cells were fixed with 4% paraformaldehyde, permeabilized with 0.1% Triton, and blocked with 1% BSA. The labeling sites were visualized by the TAMRA Fluor azide via copper(I)-catalyzed alkyne−azide cycloaddition (CuAAC). Cells were stained with Hoechst 33342 for 5 min, and mounted using VectaShield (Vector Laboratories, H-1000) for the fluorescence confocal imaging analysis.

Photo-Oxidation Labeling In Situ For RNA Analysis. The labeling procedure was the same as that in the fluorescence confocal imaging part. After blue light irradiation, cells were washed with DPBS buffer triple times, and the total cellular RNA was harvested using Trizol according to the manufacturer's instructions. Then, RNA was treated with DNase (Turbo, Thermo Fisher, cat. no. 2238) at 37 °C for 30 min and proteinase K (Invitrogen, Thermo Fisher, RNA grade cat. no. 25530049) at 42 °C for 30 min according to the protocols. The unlabeled controls were processed in the same way, except that light irradiation was omitted or TFPy was replaced by an equal volume DMSO.

CuAAC reaction was prepared with 10 μg of labeled RNA, 30 mM picolyl biotin azide to a final concentration of 2 mM, 40 mM THPTA to a final concentration of 2 mM, fresh 500 mM sodium ascorbate to a final concentration of 10 mM, and 1 mM $CuSO_4$ to a final concentration of 0.1 mM. The reactions were incubated on an orbital shaker (500 rpm) at 25 °C for 10 min. The reactions were purified by the Zymo column according to the manufacturer's instructions, and RNA was eluted in 18 μL of nuclease-free water.

RT-qPCR Analysis for Biotinylated RNA Postenrichment Based on CuAAC. Dynabeads MyOne Streptavidin C1 Beads were adopted to enrich the biotinylated RNAs upon the CuAAC reaction. Beads were prewashed with B & W buffer (1 M NaCl + 5 mM Tris pH 7.5 + 0.5 mM EDTA) triple times, washing A (0.1 M NaOH + 0.05 M NaCl) twice and washing B (0.1 M NaCl) once, and then resuspended in binding buffer (1 M NaCl + 0.2% Tween 20 + 100 mM Tris pH 7.5 + 10 mM EDTA). Then, washed beads were incubated with RNA samples at RT for 2 h with end-to-end rotation. The magnetic beads were washed with high salt wash buffer (4 M NaCl + 0.2% Tween 20 + 100 mM Tris pH 7.5 + 10 mM EDTA) triple times, 50 °C high salt wash buffer twice, and DPBS buffer twice. The enriched RNA was eluted off the beads with elution buffer (47.5 μL formamide, 1 μL 500 mM EDTA pH 8.0, 1.5 μL 50 mM D-biotin, total 50 μL for each sample) at 65 °C for 5 min and 90 °C for 5 min. The eluted RNA was purified with Trizol reagent and, upon extraction, via $CHCl_3$. The purified RNA sample was resuspended with 8 μL nuclease-free water, and 0.5 μL of the RNA solution was utilized in dot blot analysis to quality control for the enrichment process.

Eluted RNA (2 μL) from each sample was subjected to cDNA synthesis using PrimeScript Reverse Transcriptase (Takara, cat. no. 2680B) with both random hexamer and oligoT primer in 10 μL of reaction. The fold of enrichment was calculated against a no-hν negative control: $2^{\wedge}((Ct_{ENRICH\text{-no }h\nu} - Ct_{INPUT\text{-no }h\nu}) - (Ct_{ENRICH} - Ct_{INPUT}))$.

Library Preparation for High-Throughput Sequencing. The ABclonal whole RNA-seq Lib Prep Kit for Illumina (RK20306) was employed for next-generation sequencing library preparation. "Input" and "Enrich" RNA (each of 100 ng) first underwent the rRNA-depletion step and then were processed accordingly.

■ ASSOCIATED CONTENT

Supporting Information

The Supporting Information is available free of charge at https://pubs.acs.org/doi/10.1021/acschembio.3c00617.

Biochemical methods, synthetic characterizations, DFT computation setting, and supporting figures (PDF)

■ AUTHOR INFORMATION

Corresponding Author

Ying Li − *Department of Chemistry, The University of Hong Kong, Hong Kong 999077, China; Laboratory for Synthetic Chemistry and Chemical Biology Limited, Hong Kong 999077, China;* orcid.org/0000-0002-0438-449X; Email: yingli0e@hku.hk

Authors

Jiying Liang − *Department of Chemistry, The University of Hong Kong, Hong Kong 999077, China*

Jinghua Han − *Department of Chemistry, The University of Hong Kong, Hong Kong 999077, China*

Yuan Zhuang − *Department of Chemistry, The University of Hong Kong, Hong Kong 999077, China; Hong Kong Quantum AI Lab Limited, Hong Kong 999077, China;* orcid.org/0009-0009-6202-3092

GuanHua Chen − *Department of Chemistry, The University of Hong Kong, Hong Kong 999077, China; Hong Kong Quantum AI Lab Limited, Hong Kong 999077, China;* orcid.org/0000-0001-5015-0902

Complete contact information is available at: https://pubs.acs.org/10.1021/acschembio.3c00617

Author Contributions

J.L. conceived the project and conducted all the experiments except computational analysis. J.H. performed bioinformatic analysis. Y.Z. performed DFT computational studies under the guidance of G.C. Y.L. supervised the project. J.L. wrote the original draft and edited the manuscript with Y.L. All the authors reviewed the manuscript.

Notes

The authors declare no competing financial interest.

■ ACKNOWLEDGMENTS

This work was financially supported by Hong Kong Research Grants Council (ECS 27302220; GRF 17318422, 17309620), the National Science Fund of China (22107088), the Laboratory for Synthetic Chemistry and Chemical Biology under the Health@InnoHK Program launched by the Innovation and Technology Commission (Hong Kong, China), and Hong Kong Quantum AI Lab Limited, AIR@InnoHK of the Hong Kong Government. RNA sequencing data analysis was conducted on HKU High-Performance Computing infrastructure maintained by the Information Technology Services at the University of Hong Kong (HKU).

■ REFERENCES

(1) Buxbaum, A. R.; Haimovich, G.; Singer, R. H. In the right place at the right time: Visualizing and understanding mRNA localization. *Nat. Rev. Mol. Cell Biol.* **2015**, *16*, 95−109.

(2) Chin, A.; Lecuyer, E. RNA localization: Making its way to the center stage. *Biochim Biophys Acta Gen Subj* **2017**, *1861*, 2956−2970.

(3) Zhou, Y.; Zou, P. The evolving capabilities of enzyme-mediated proximity labeling. *Curr. Opin. Chem. Biol.* **2021**, *60*, 30−38.

(4) Kang, M. G.; Rhee, H. W. Molecular spatiomics by proximity labeling. *Acc. Chem. Res.* **2022**, *55*, 1411−1422.

(5) Fazal, F. M.; Han, S.; Parker, K. R.; Kaewsapsak, P.; Xu, J.; Boettiger, A. N.; Chang, H. Y.; Ting, A. Y. Atlas of subcellular RNA localization revealed by APEX-seq. *Cell* **2019**, *178*, 473−490.

(6) Engel, K. L.; Lo, H. Y. G.; Goering, R.; Li, Y.; Spitale, R. C.; Taliaferro, J. M. Analysis of subcellular transcriptomes by RNA proximity labeling with Halo-seq. *Nucleic Acids Res.* **2022**, *50*, No. e24.

(7) Wang, P. C.; Tang, W.; Li, Z. Y.; Zou, Z. Y.; Zhou, Y.; Li, R.; Xiong, T. Y.; Wang, J. B.; Zou, P. Mapping spatial transcriptome with light-activated proximity-dependent RNA labeling. *Nat. Chem. Biol.* **2019**, *15*, 1110−1119.
(8) Li, Y.; Aggarwal, M. B.; Nguyen, K.; Ke, K.; Spitale, R. C. Assaying RNA localization in situ with spatially restricted nucleobase oxidation. *ACS Chem. Biol.* **2017**, *12*, 2709−2714.
(9) Wang, H.; Wang, Z.; Gao, H.; Liu, J.; Qiao, Z.; Zhao, B.; Liang, Z.; Jiang, B.; Zhang, L.; Zhang, Y. A photo-oxidation driven proximity labeling strategy enables profiling of mitochondrial proteome dynamics in living cells. *Chem. Sci.* **2022**, *13*, 11943−11950.
(10) Li, L.; Liang, J. Y.; Luo, H.; Tam, K. M.; Tse, E. C. M.; Li, Y. A new chemical approach for proximity labelling of chromatin-associated rnas and proteins with visible light irradiation. *Chem. Commun.* **2019**, *55*, 12340−12343.
(11) Tamura, T.; Takato, M.; Shiono, K.; Hamachi, I. Development of a photoactivatable proximity labeling method for the identification of nuclear proteins. *Chem. Lett.* **2020**, *49*, 145−148.
(12) Mercer, T. R.; Neph, S.; Dinger, M. E.; Crawford, J.; Smith, M. A.; Shearwood, A. M. J.; Haugen, E.; Bracken, C. P.; Rackham, O.; Stamatoyannopoulos, J. A.; Filipovska, A.; Mattick, J. S. The human mitochondrial transcriptome. *Cell* **2011**, *146*, 645−658.
(13) Ren, B.; Guan, M. X.; Zhou, T.; Cai, X.; Shan, G. Emerging functions of mitochondria-encoded noncoding RNAs. *Trends Genet.* **2023**, *39*, 125−139.
(14) Friedman, J. R.; Nunnari, J. Mitochondrial form and function. *Nature* **2014**, *505*, 335−343.
(15) O'Rourke, B. Beyond the power of mitochondria. *Nat. Rev. Cardiol* **2016**, *13*, 386−388.
(16) Dong, Y. R.; Yoshitomi, T.; Hu, J. F.; Cui, J. Z. Long noncoding RNAs coordinate functions between mitochondria and the nucleus. *Epigenet. Chromatin* **2017**, *10*, 41.
(17) Jeandard, D.; Smirnova, A.; Tarassov, I.; Barrey, E.; Smirnov, A.; Entelis, N. Import of non-coding RNAs into human mitochondria: A critical review and emerging approaches. *Cells* **2019**, *8*, 286.
(18) Sang, L. J.; Ju, H. Q.; Yang, Z. Z.; Ge, Q. W.; Zhang, Z.; Liu, F. Z.; Yang, L. J.; Gong, H. D.; Shi, C. Y.; Qu, L.; Chen, H.; Wu, M. J.; Chen, H.; Li, R. H.; Zhuang, Q. Q.; Piao, H. L.; Yan, Q. F.; Yu, W. S.; Wang, L. J.; Shao, J. Z.; et al. Mitochondrial long non-coding RNA GAS5 tunes TCA metabolism in response to nutrient stress. *Nat. Metab.* **2021**, *3*, 90−106.
(19) Kaewsapsak, P.; Shechner, D. M.; Mallard, W.; Rinn, J. L.; Ting, A. Y. Live-cell mapping of organelle-associated RNAs via proximity biotinylation combined with protein-RNA crosslinking. *Elife* **2017**, *6*, No. e29224.
(20) Wang, H. W.; Fang, B.; Peng, B.; Wang, L. M.; Xue, Y. F.; Bai, H.; Lu, S. C.; Voelcker, N. H.; Li, L.; Fu, L.; Huang, W. Recent advances in chemical biology of mitochondria targeting. *Front. Chem.* **2021**, *9*, No. 683220.
(21) Guo, X. L.; Yang, N. D.; Ji, W. H.; Zhang, H.; Dong, X.; Zhou, Z. Q.; Li, L.; Shen, H. M.; Yao, S. Q.; Huang, W. Mito-bomb: Targeting mitochondria for cancer therapy. *Adv. Mater.* **2021**, *33*, No. 2007778.
(22) Qu, R.; Zhen, X.; Jiang, X. Q. Emerging designs of aggregation-induced emission agents for enhanced phototherapy applications. *CCS Chemistry* **2022**, *4*, 401−419.
(23) Hu, F.; Xu, S. D.; Liu, B. Photosensitizers with aggregation-induced emission: Materials and biomedical applications. *Adv. Mater.* **2018**, *30*, No. 1801350.
(24) Ni, J. C.; Wang, Y. J.; Zhang, H. K.; Sun, J. Z.; Tang, B. Z. Aggregation-induced generation of reactive oxygen species: Mechanism and photosensitizer construction. *Molecules* **2021**, *26*, 268.
(25) Wang, D.; Lee, M. M. S.; Shan, G. G.; Kwok, R. T. K.; Lam, J. W. Y.; Su, H. F.; Cai, Y. C.; Tang, B. Z. Highly efficient photosensitizers with far-red/near-infrared aggregation-induced emission for in vitro and in vivo cancer theranostics. *Adv. Mater.* **2018**, *30*, No. 1802105.
(26) Xu, W. H.; Lee, M. M. S.; Nie, J. J.; Zhang, Z. H.; Kwok, R. T. K.; Lam, J. W. Y.; Xu, F. J.; Wang, D.; Tang, B. Three-pronged attack by homologous far-red/NIR AIEgens to achieve 1 + 1+1 > 3 synergistic enhanced photodynamic therapy. *Angew. Chem., Int. Ed.* **2020**, *59*, 9610−9616.
(27) Chen, S. H.; Chen, Q.; Luo, S. H.; Cao, X. Y.; Yang, G. X.; Zeng, X. Q.; Wang, Z. Y. Progress in design, synthesis and application of triphenylamine-based fluorescent probes. *Chinese. J. Org. Chem.* **2021**, *41*, 919−933.
(28) Jeong, J. H.; Kim, J. S.; Campo, J.; Lee, S. H.; Jeon, W. Y.; Wenseleers, W.; Jazbinsek, M.; Yun, H.; Kwon, O. P. N-methylquinolinium derivatives for photonic applications: Enhancement of electron-withdrawing character beyond that of the widely-used n-methylpyridinium. *Dyes Pigm.* **2015**, *113*, 8−17.
(29) Zheng, B.; Huo, L. J. Recent advances of furan and its derivatives based semiconductor materials for organic photovoltaics. *Small Methods* **2021**, *5*, No. 2100493.
(30) Delgado, M. C. R.; Hernandez, V.; Casado, J.; Navarrete, J. T. L.; Raimundo, J. M.; Blanchard, P.; Roncali, J. Vibrational and quantum-chemical study of push-pull chromophores for second-order nonlinear optics from rigidified thiophene-based π-conjugating spacers. *Chem.—Eur. J.* **2003**, *9*, 3670−3682.
(31) Lu, B.; Huang, Y. Y.; Zhang, Z. C.; Quan, H.; Yao, Y. Organic conjugated small molecules with donor-acceptor structures: Design and application in the phototherapy of tumors. *Mater. Chem. Front.* **2022**, *6*, 2968−2993.
(32) Xiong, W.; Wang, L. Y.; Chen, X. L.; Tang, H.; Cao, D. R.; Zhang, G. Z.; Chen, W. Pyridinium-substituted tetraphenylethylene salt-based photosensitizers by varying counter anions: A highly efficient photodynamic therapy for cancer cell ablation and bacterial inactivation. *J. Mater. Chem. B* **2020**, *8*, 5234−5244.
(33) Liang, J. M.; Wu, P.; Tan, C. Y.; Jiang, Y. Y. White light-induced cell apoptosis by a conjugated polyelectrolyte through singlet oxygen generation. *RSC Adv.* **2018**, *8*, 9218−9222.
(34) Castano, A. P.; Demidova, T. N.; Hamblin, M. R. Mechanisms in photodynamic therapy: Part one-photosensitizers, photochemistry and cellular localization. *Photodiagnosis Photodyn. Ther.* **2004**, *1*, 279−293.
(35) Baptista, M. S.; Cadet, J.; Di Mascio, P.; Ghogare, A. A.; Greer, A.; Hamblin, M. R.; Lorente, C.; Nunez, S. C.; Ribeiro, M. S.; Thomas, A. H.; Vignoni, M.; Yoshimura, T. M. Type i and type ii photosensitized oxidation reactions: Guidelines and mechanistic pathways. *Photochem. Photobiol.* **2017**, *93*, 912−919.
(36) Casida, M. E.; Huix-Rotllant, M. Progress in time-dependent density-functional theory. *Annu. Rev. Phys. Chem.* **2012**, *63*, 287−323.
(37) Yuan, G.; Lv, C.; Liang, J. C.; Zhong, X. X.; Li, Y.; He, J. C.; Zhao, A. J.; Li, L.; Shao, Y. H.; Zhang, X. H.; Wang, S. F.; Cheng, Y.; He, H. P. Molecular engineering of efficient singlet oxygen generators with near-infrared AIE features for mitochondrial targeted photodynamic therapy. *Adv. Funct. Mater.* **2021**, *31*, No. 2104026.
(38) Deiana, M.; Josse, P.; Dalinot, C.; Osmolovskyi, A.; Marques, P. S.; Castan, J. M. A.; Galan, L. A.; Allain, M.; Khrouz, L.; Maury, O.; Le Bahers, T.; Blanchard, P.; Dabos-Seignon, S.; Monnereau, C.; Sabouri, N.; Cabanetos, C. Site-selected thionated benzothioxanthene chromophores as heavy-atom-free small-molecule photosensitizers for photodynamic therapy. *Commun. Chem.* **2022**, *5*, 142.
(39) Mosquera, J.; Garcia, I.; Liz-Marzan, L. M. Cellular uptake of nanoparticles versus small molecules: A matter of size. *Acc. Chem. Res.* **2018**, *51*, 2305−2313.
(40) Cottet-Rousselle, C.; Ronot, X.; Leverve, X.; Mayol, J. F. Cytometric assessment of mitochondria using fluorescent probes. *Cytometry Part A* **2011**, *79a*, 405−425.
(41) Wilkinson, F.; Brummer, J. G. Rate constants for the decay and reactions of the lowest electronically excited singlet-state of molecular-oxygen in solution. *J. Phys. Chem. Ref. Data* **1981**, *10*, 809−1000.
(42) Nonell, S.; Moncayo, L.; Trull, F.; Amatguerri, F.; Lissi, E. A.; Soltermann, A. T.; Criado, S.; Garcia, N. A. Solvent influence on the kinetics of the photodynamic degradation of trolox, a water-soluble model-compound for vitamin-E. *J. Photochem. Photobiol. B: Biol.* **1995**, *29*, 157−162.

https://doi.org/10.1021/acschembio.3c00617
ACS Chem. Biol. XXXX, XXX, XXX−XXX

(43) Liubimovskii, S. O.; Ustynyuk, L. Y.; Tikhonov, A. N. Superoxide radical scavenging by sodium 4,5-dihydroxybenzene-1,3-disulfonate dissolved in water: Experimental and quantum chemical studies. *J. Mol. Liq.* **2021**, *333*, No. 115810.
(44) Goldstein, S.; Czapski, G. Mannitol as an OH scavenger in aqueous-solutions and in biological-systems. *Int. J. Radiat. Biol.* **1984**, *46*, 725−729.
(45) Shestakova, E. A.; Singer, R. H.; Condeelis, J. The physiological significance of beta-actin mRNA localization in determining cell polarity and directional motility. *Proc. Natl. Acad. Sci. U. S. A.* **2001**, *98*, 7045−7050.
(46) Sirover, M. A. Subcellular dynamics of multifunctional protein regulation: Mechanisms of GAPDH intracellular translocation. *J. Cell. Biochem.* **2012**, *113*, 2193−2200.
(47) Prasanth, K. V.; Camiolo, M.; Chan, G.; Tripathi, V.; Denis, L.; Nakamura, T.; Hubner, M. R.; Spector, D. L. Nuclear organization and dynamics of 7SK RNA in regulating gene expression. *Mol. Biol. Cell* **2010**, *21*, 4184−4196.
(48) Nitzahn, M.; Lipshutz, G. S. CPS1: Looking at an ancient enzyme in a modern light. *Mol. Genet. Metab.* **2020**, *131*, 289−298.
(49) Wang, C. G.; Taki, M.; Sato, Y.; Tamura, Y.; Yaginuma, H.; Okada, Y.; Yamaguchi, S. A photostable fluorescent marker for the superresolution live imaging of the dynamic structure of the mitochondrial cristae. *Proc. Natl. Acad. Sci. U. S. A.* **2019**, *116*, 15817−15822.
(50) Chen, Q. X.; Fang, H. B.; Shao, X. T.; Tian, Z. Q.; Geng, S. S.; Zhang, Y. M.; Fan, H. X.; Xiang, P.; Zhang, J.; Tian, X. H.; Zhang, K.; He, W. J.; Guo, Z. J.; Diao, J. J. A dual-labeling probe to track functional mitochondria-lysosome interactions in live cells. *Nat. Commun.* **2020**, *11*, 6290.
(51) Perkins, G.; Renken, C.; Martone, M. E.; Young, S. J.; Ellisman, M. Electron tomography of neuronal mitochondria: Three-dimensional structure and organization of cristae and membrane contacts. *J. Struct. Biol.* **1997**, *119*, 260−272.
(52) Kuhlbrandt, W. Structure and function of mitochondrial membrane protein complexes. *BMC Biol.* **2015**, *13*, 89.
(53) Moan, J. On the diffusion length of singlet oxygen in cells and tissues. *J. Photochem. Photobiol. B: Biol.* **1990**, *6*, 343−347.
(54) Colombini, M. A candidate for the permeability pathway of the outer mitochondrial membrane. *Nature* **1979**, *279*, 643−645.
(55) Xian, H. X.; Liou, Y. C. Functions of outer mitochondrial membrane proteins: Mediating the crosstalk between mitochondrial dynamics and mitophagy. *Cell Death Differ.* **2021**, *28*, 827−842.
(56) Ellenrieder, L.; Rampelt, H.; Becker, T. Connection of protein transport and organelle contact sites in mitochondria. *J. Mol. Biol.* **2017**, *429*, 2148−2160.
(57) Zheng, F.; Zhou, X.; Zou, P.; Yu, C. Genetically encoded photocatalytic protein labeling enables spatially-resolved profiling of intracellular proteome. *Nat. Commun.* **2023**, *14*, 2978.

https://doi.org/10.1021/acschembio.3c00617
ACS Chem. Biol. XXXX, XXX, XXX−XXX